

Dependence of Rayleigh-Taylor instability of finite-thickness shell on initial perturbed wavelengths

Hong-Yu Guo(郭宏宇), Ben-Jin Guan(关本金), Li-Feng Wang(王立锋), Zhi-Yuan Li(李志远), and Ying-Jun Li(李英骏)

Citation: Chin. Phys. B, 2025, 34 (**11**): 115202. DOI: 10.1088/1674-1056/ade06b

Chttp://cpb.iphy.ac.cn; http://iopscience.iop.org/cpb

What follows is a list of articles you may be interested in

Scaling of rise time of drive current on development of magneto-Rayleigh-Taylor instabilities for single-shell Z-pinches

Xiaoguang Wang(王小光), Guanqiong Wang(王冠琼), Shunkai Sun(孙顺凯), Delong Xiao(肖德龙), Ning Ding(丁宁), Chongyang Mao(毛重阳), and Xiaojian Shu(束小建)

Chin. Phys. B, 2022, 31 (**2**): 025203. DOI: 10.1088/1674-1056/ac1fd9

Weakly nonlinear multi-mode Bell–Plesset growth in cylindrical geometry

Hong-Yu Guo(郭宏宇), Tao Cheng(程涛), and Ying-Jun Li(李英骏)

Chin. Phys. B, 2020, 29 (**11**): 115202. DOI: 10.1088/1674-1056/ab9c14

Numerical study on magneto-Rayleigh-Taylor instabilities for thin liner implosions on the primary test stand facility

Xiao-Guang Wang(王小光), Shun-Kai Sun(孙顺凯), De-Long Xiao(肖德龙), Guan-Qiong Wang(王冠琼), Yang Zhang(张扬), Shao-Tong Zhou(周少彤), Xiao-Dong Ren(任晓东), Qiang Xu(徐强), Xian-Bin Huang(黄显宾), Ning Ding(丁宁), Xiao-Jian Shu(束小建)

Chin. Phys. B, 2019, 28 (**3**): 035201. DOI: 10.1088/1674-1056/28/3/035201

Coupling between velocity and interface perturbations in cylindrical Rayleigh-Taylor instability

Hong-Yu Guo(郭宏宇), Li-Feng Wang(王立锋), Wen-Hua Ye(叶文华), Jun-Feng Wu(吴俊峰), Wei-Yan Zhang(张维岩)

Chin. Phys. B, 2018, 27 (**5**): 055205. DOI: 10.1088/1674-1056/27/5/055205

Rayleigh-Taylor instability at spherical interfaces of incompressible fluids

Hong-Yu Guo(郭宏宇), Li-Feng Wang(王立锋), Wen-Hua Ye(叶文华), Jun-Feng Wu(吴俊峰), Ying-Jun Li(李英骏), Wei-Yan Zhang(张维岩)

Chin. Phys. B, 2018, 27 (**2**): 025206. DOI: 10.1088/1674-1056/27/2/025206

Dependence of Rayleigh–Taylor instability of finite-thickness shell on initial perturbed wavelengths

Hong-Yu Guo(郭宏宇)[1,†], Ben-Jin Guan(关本金)[1,2,†,‡], Li-Feng Wang(王立锋)[2,3], Zhi-Yuan Li(李志远)[2], and Ying-Jun Li(李英骏)[1,§]

[1] *State Key Laboratory for Tunnel Engineering, China University of Mining and Technology, Beijing* 100083, *China*
[2] *Institute of Applied Physics and Computational Mathematics, Beijing* 100094, *China*
[3] *Center for Applied Physics and Technology, HEDPS, and College of Engineering, Peking University, Beijing* 100871, *China*

(Received 30 March 2025; revised manuscript received 26 May 2025; accepted manuscript online 4 June 2025)

Rayleigh–Taylor instability (RTI) of finite-thickness shell significantly impacts shell deformation and material mixing processes, with crucial implications for inertial confinement fusion (ICF). This study focuses on the RTI growth at the dual interfaces of a thin shell. A second-order weakly nonlinear (WN) analytical theory is developed to investigate the nonlinear deformation of the shell induced by different perturbation wavelengths initially imposed at the upper and lower interfaces. The validity of the theoretical results within the WN regime has been confirmed via two-dimensional Eulerian numerical simulations. Due to the interface coupling effect, the initially imposed single-mode perturbations at the upper and lower interfaces progressively evolve, exhibiting characteristics typical of multi-mode perturbations. When the initial perturbation wavelengths differ significantly, the primary structure of RTI retains its integrity, a behavior attributed to the dominance of long-wavelength perturbations. For comparable initial wavelengths, mode-coupling significantly distorts the bubble-spike structure in RTI, with the thin shell becoming prone to rupture due to enhanced nonlinear interactions.

Keywords: Rayleigh–Taylor instability, mode-coupling, inertial confinement fusion

PACS: 52.57.Fg, 47.20.Ma, 52.35.Py

DOI: 10.1088/1674-1056/ade06b **CSTR:** 32038.14.CPB.ade06b

1. Introduction

Rayleigh–Taylor instability (RTI)[1,2] occurs when the heavier fluid is accelerated or supported by the lighter fluid. The small perturbations at the interface between two fluids will grow with time, leading to significant deformation of the fluid interface and mixing of the material. RTI plays a key role in the evolution of astronomical phenomenon, such as supernova explosions[3] and the process of inertial confinement fusion (ICF).[4,5] Understanding and controlling the growth of RTI is critical to the success of the high-gain implosion experiments, which have just achieved a milestone in its goal of clean energy applications.[6]

In ICF, a central ignition capsule consists of two fluid layers, with an imploded fuel shell distributed inside and an ablative layer surrounding the outside. Therefore, the implosion capsule has at least three interfaces, namely, the ablative interface, the fuel-ablator interface, and the hot-spot interface. During the implosion acceleration stage, the ablative interface between the high-density fuel shell and ablated plasma is strongly affected by RTI, where the fuel shell is accelerated by the ablative plasma. During the deceleration phase, the hot-spot interface is likewise influenced by RTI. At this time, the low-density hot-spot decelerates the heavy shell, potentially leading to the development of RTI. The growth of RTI can lead to the mixing of ablative materials into the hot-spot. This limits the implosion compression of fuel, compromises the integrity of the imploding shell, and ultimately degrades the performance of ICF. Due to its importance and significance to the basic research and engineering application of ICF implosion, studying the growth of RTI in ICF implosion remains a key issue.[7,8]

The classical RTI (CRTI) for inviscid and immiscible fluids was first initially investigated by Rayleigh[1] and Taylor,[2] the linear growth of two semi-infinity fluids is derived analytically. Research has shown that the interface perturbations at fluid interface grow exponentially with time, *i.e.*, $\eta(t) \sim \eta_0 \mathrm{e}^{\gamma t}$. Here $\gamma = \sqrt{Akg}$ represents the linear growth rate, η_0 is the initial amplitude of interface perturbations, A is the Atwood number at the interface, k is wave-number, and g is the gravitational acceleration. Due to its critical significance in ICF, RTI has been extensively studied over the past few decades. Most researchers have explored the RTI model for two semi-infinite fluids separated by a single interface, taking various effects into consideration.[9–15] However, this study aims to delve into the instability growth of the accelerated shell interface during ICF implosion. Understanding how perturba-

† These authors contributed equally to this work.
‡Corresponding author. E-mail: bjguanshandong@163.com
§Corresponding author. E-mail: lyj@aphy.iphy.ac.cn

© 2025 Chinese Physical Society and IOP Publishing Ltd. All rights, including for text and data mining, AI training, and similar technologies, are reserved.

tions on one interface couple with those on the other is a crucial aspect in the ICF implosion process. Mikaelian[16–18] conducted research on the linear growth of RTI across an arbitrary number of stratified fluids. Through analytical approaches, the study delved into the interface coupling effects and linear growth rates of three-fluid systems with two interfaces. We further extended the model and studied the linear growth of RTI in planar,[19] cylindrical,[20] and spherical geometries,[21] the explicit interface coupling phenomenons in different geometries are analyzed. The RTI growth on a finite plasma slab interface with an arbitrary magnitude magnetic field is considered by Weis,[22] the feedback factor between two interfaces of the plasma slab was analyzed through theoretical and experimental comparisons. Velikovich[23] discussed Bell–Plesset effects in the RTI growth of finite-thickness shell in spherical and cylindrical geometries. Analytical derivations were carried out to obtain equations describing the time-dependent dispersion of the instantaneous growth rate. This is applicable under the condition where the perturbation amplitude $\eta(t)$ remains significantly smaller than the wavelength λ ($\eta(t) \ll \lambda$), which is consistent with the experiment results.[24,25] As the amplitude of the perturbation grows to a magnitude comparable to the perturbation wavelength, such that $k\eta(t) \sim 1$, the perturbation starts to transition into the weakly nonlinear (WN) stage. The initially symmetric interface will evolve into an irregular bubble-spike structure. Significantly, the WN model can reveals the mode-coupling process, along with the physical mechanisms of how perturbations progress from the linear to the nonlinear stage. For instance, the generation of the second harmonic may trigger asymmetric interface deformation. The three-dimensional CRTI with different interface symmetries (rectangular, circular, and hexagonal) was analyzed by Jacobs[9] through a third-order WN model for $A = 1$. The study revealed that perturbation waveforms featuring axial symmetry exhibit the most rapid growth. The WN model was extended to planar geometry,[11] cylindrical geometry,[12] and spherical geometry[13] for arbitrary Atwood number A. Due to the influence of geometric effects, the results of cylindrical geometry are slightly different from those of planar geometry. However, the analytical solutions in spherical geometry are quite different from those in plane geometry. It is found that a wide mode spectrum is generated through a single-mode perturbation in spherical geometry. The WN evolution of RTI in finite-thickness shell was discussed analytically.[26,27] This model clearly depicted the deformation of the thin shell and the feedback characteristics between the two interfaces. Recently, the effect of initial phase on the RTI of a finite-thickness fluid shell was investigated via the third-order WN model.[28] The positions of bubble-spike structures are affected by the initial phase difference of the perturbations at two interfaces. All these works focus on perturbations at the shell interfaces with the same wavelength. However, due to the inhomogeneity of the imploded shell and the asymmetry of the laser driving, the perturbation wavelengths at the two interfaces usually differ. The evolution of RTI is influenced by small-scale details of the initial perturbation wavelengths until late nonlinear stage. In this paper, we investigate RTI growth in a finite-thickness shell during the WN stage, where each interface exhibits a distinct perturbation wavelength at the initial.

This paper is organized as follows. Section 2 describes the theoretical model and derives the second-order solutions for RTI growth. The physical models for the simulation of the RTI are presented in Section 3. Section 4 displays the interface deformation and mode-coupling characteristics. The numerical results are also displayed. Section 5 summarizes the major results and gives some conclusions.

2. Theoretical model and mathematical formulation

As shown in Fig. 1, an incompressible, irrotational, inviscid, and immiscible fluid slab is immersed in a gravitational field $-g\hat{e}_y$. The density of the fluid is ρ, and the shell thickness is represented by d. Two-dimensional Cartesian coordinate is established, where x and y represent the directions along and normal to the lower interface of the fluid shell, respectively. The initial unperturbed lower and upper interfaces are located at $y = 0$ and d, respectively. In the following discussion, the physical quantities on the upper interface are represented by the superscript "u" and the quantities on the lower interface are represented by superscript "l", unless otherwise specified.

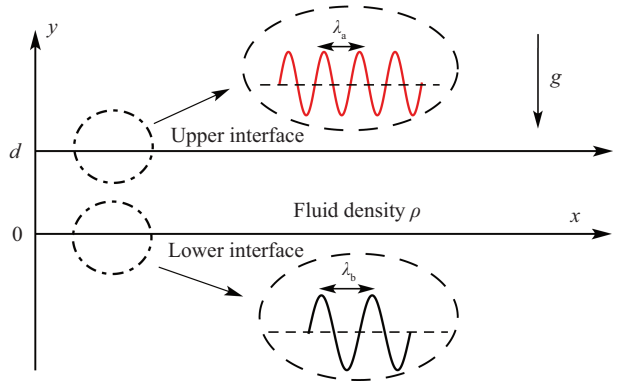


Fig. 1. Schematic drawing of the finite-thickness fluid slab perturbed with different wavelengths at the upper and lower interfaces.

The velocity potential theory is used to describe the incompressible fluid layer, so the velocity potential for an incompressible fluid can be expressed as

$$\Phi(x,y,t) = \Phi_0(t) + \varphi(x,y,t), \tag{1}$$

where $\Phi_0(t)$ and $\varphi(x,y,t)$ are perturbed and unperturbed velocity potential, respectively. The pressure conditions at the

upper and lower interfaces are governed by the Bernoulli equation which can be written as

$$P^{\mathrm{u}}_{(0)} + \tilde{p}^{\mathrm{u}} = -\rho\left[\Phi_t + \frac{1}{2}(\nabla\Phi)^2 + g\eta^{\mathrm{u}} + gd + f(t)\right], \quad (2)$$

$$P^{\mathrm{l}}_{(0)} + \tilde{p}^{\mathrm{l}} = -\rho\left[\Phi_t + \frac{1}{2}(\nabla\phi)^2 + g\eta^{\mathrm{l}} + f(t)\right], \quad (3)$$

where $P^{\mathrm{u}}_{(0)}$ and $P^{\mathrm{l}}_{(0)}$ are the unperturbed pressures at the two interfaces. As can be seen, the equilibrium pressure condition $P^{\mathrm{l}}_{(0)} - P^{\mathrm{u}}_{(0)} = \rho g d$ has been satisfied for the unperturbed pressures. Thus, the perturbed pressured can be obtained as

$$\tilde{p}^i = -\rho\left[\varphi_t + \frac{1}{2}\left(\varphi_x^2 + \varphi_y^2\right) + g\eta^i\right], \quad (4)$$

where $i = \mathrm{u}, \mathrm{l}$ represent the physical quantities at the upper and lower interfaces. The perturbed pressures at the two interfaces are zero for a finite-thickness fluid layer,[26–28] namely, $\tilde{p}^i = 0$. The kinematic conditions at the upper and lower interfaces are expressed as

$$\eta^i_t + \varphi_x \cdot \eta^i_x - \varphi_y = 0, \quad (5)$$

which means the normal components of velocity should be equal to the normal component of fluid velocity. Considering there are perturbations with different wavelengths at the two interfaces of the shell at the initial time. The upper interface is initially perturbed with wave-number k_{a} ($k_{\mathrm{a}} = 2\pi/\lambda_{\mathrm{a}}$), and the lower interface is perturbed with wave-number k_{b} ($k_{\mathrm{b}} = 2\pi/\lambda_{\mathrm{b}}$).

Then, the perturbations and perturbed velocity potential are expanded as

$$\eta^{\mathrm{u}}(x,t) = \sum_i\sum_j \varepsilon^i \eta_i^{\mathrm{u},j}(t)\cos(k_j x), \quad (6)$$

$$\eta^{\mathrm{l}}(x,t) = \sum_i\sum_j \varepsilon^i \eta_i^{\mathrm{l},j}(t)\cos(k_j x), \quad (7)$$

$$\varphi(x,y,t) = \sum_i\sum_j \varepsilon^i \left[A_i^j(t)\,\mathrm{e}^{k_j y} + B_i^j(t)\,\mathrm{e}^{-k_j y}\right]\cos(k_j x), \quad (8)$$

where the laplace equation $\nabla^2\varphi = 0$ has been satisfied. We now substitute Eqs. (6)–(8) into Eqs. (4) and (5), then, we can generate a series of power expansions of the governing equation at $y = 0$ and $y = d$. We then collect the terms featuring the same power of the parameter ε^n, thereby we can establish a series of governing equations. Once these equations are obtained, we can set $\varepsilon = 1$. This enables us to solve these equations step-by-step easier.

At the first-order $O(\varepsilon)$, the governing equations for $\eta_1^{\mathrm{u,a}}$, $\eta_1^{\mathrm{u,b}}$, $\eta_1^{\mathrm{l,a}}$, and $\eta_1^{\mathrm{l,b}}$ are given below:

$$\frac{\mathrm{d}^2\eta_1^{\mathrm{u,a}}}{\mathrm{d}t^2} - \frac{2\mathrm{e}^{-\xi_{\mathrm{a}}}}{1+\mathrm{e}^{-2\xi_{\mathrm{a}}}}\frac{\mathrm{d}^2\eta_1^{\mathrm{l,a}}}{\mathrm{d}t^2} + \gamma_{\mathrm{a}}^2\frac{1-\mathrm{e}^{-2\xi_{\mathrm{a}}}}{1+\mathrm{e}^{-2\xi_{\mathrm{a}}}}\eta_1^{\mathrm{u,a}} = 0, \quad (9)$$

$$\frac{\mathrm{d}^2\eta_1^{\mathrm{u,b}}}{\mathrm{d}t^2} - \frac{2\mathrm{e}^{-\xi_{\mathrm{b}}}}{1+\mathrm{e}^{-2\xi_{\mathrm{b}}}}\frac{\mathrm{d}^2\eta_1^{\mathrm{l,b}}}{\mathrm{d}t^2} + \gamma_{\mathrm{b}}^2\frac{1-\mathrm{e}^{-2\xi_{\mathrm{b}}}}{1+\mathrm{e}^{-2\xi_{\mathrm{b}}}}\eta_1^{\mathrm{u,b}} = 0, \quad (10)$$

$$\frac{\mathrm{d}^2\eta_1^{\mathrm{l,a}}}{\mathrm{d}t^2} - \frac{2\mathrm{e}^{-\xi_{\mathrm{a}}}}{1+\mathrm{e}^{-2\xi_{\mathrm{a}}}}\frac{\mathrm{d}^2\eta_1^{\mathrm{u,a}}}{dt^2} - \gamma_{\mathrm{a}}^2\frac{1-\mathrm{e}^{-2\xi_{\mathrm{a}}}}{1+\mathrm{e}^{-2\xi_{\mathrm{a}}}}\eta_1^{\mathrm{l,a}} = 0, \quad (11)$$

$$\frac{\mathrm{d}^2\eta_1^{\mathrm{l,b}}}{\mathrm{d}t^2} - \frac{2\mathrm{e}^{-\xi_{\mathrm{b}}}}{1+\mathrm{e}^{-2\xi_{\mathrm{b}}}}\frac{\mathrm{d}^2\eta_1^{\mathrm{u,b}}}{\mathrm{d}t^2} - \gamma_{\mathrm{b}}^2\frac{1-\mathrm{e}^{-2\xi_{\mathrm{b}}}}{1+\mathrm{e}^{-2\xi_{\mathrm{b}}}}\eta_1^{\mathrm{l,b}} = 0, \quad (12)$$

where $\gamma_{\mathrm{a}}^2 = k_{\mathrm{a}}g$ and $\gamma_{\mathrm{b}}^2 = k_{\mathrm{b}}g$ are the linear growth rate of the two wavelengths. The $\xi_{\mathrm{a}} = k_{\mathrm{a}}d$ and $\xi_{\mathrm{b}} = k_{\mathrm{b}}d$ are the normalized shell thickness.

Considering that single-mode cosinusoidal perturbations with different wavelengths exist at the upper interface (with mode-number k_{a}) and the lower interface (with mode-number k_{b}), which can be expressed as

$$\eta^{\mathrm{u}}(x,t=0) = u_{\mathrm{a}}\cos(k_{\mathrm{a}}x), \quad (13)$$

$$\eta^{\mathrm{l}}(x,t=0) = l_{\mathrm{b}}\cos(k_{\mathrm{b}}x). \quad (14)$$

Thus, the linear growth of interface perturbation can be obtained as

$$\eta_1^{\mathrm{u,a}} = \Xi_{\mathrm{a}}\left[\cos(\Gamma_{\mathrm{a}}) - \mathrm{e}^{-2\xi_{\mathrm{a}}}\cosh(\Gamma_{\mathrm{a}})\right], \quad (15)$$

$$\eta_1^{\mathrm{l,a}} = \Xi_{\mathrm{a}}\,\mathrm{e}^{-\xi_{\mathrm{a}}}\left[\cos(\Gamma_{\mathrm{a}}) - \cosh(\Gamma_{\mathrm{a}})\right], \quad (16)$$

$$\eta_1^{\mathrm{u,b}} = \Xi_{\mathrm{b}}\,\mathrm{e}^{-\xi_{\mathrm{b}}}\left[\cosh(\Gamma_{\mathrm{b}}) - \cos(\Gamma_{\mathrm{b}})\right], \quad (17)$$

$$\eta_1^{\mathrm{l,b}} = \Xi_{\mathrm{b}}\left[\cosh(\Gamma_{\mathrm{b}}) - \mathrm{e}^{-2\xi_{\mathrm{b}}}\cos(\Gamma_{\mathrm{b}})\right], \quad (18)$$

where $\Gamma_{\mathrm{a}} = \gamma_{\mathrm{a}}t$ and $\Gamma_{\mathrm{b}} = \gamma_{\mathrm{b}}t$ are the normalized growth rates. The coefficients are $\Xi_{\mathrm{a}} = u_{\mathrm{a}}/(1-\mathrm{e}^{-2\xi_{\mathrm{a}}})$ and $\Xi_{\mathrm{b}} = l_{\mathrm{b}}/(1-\mathrm{e}^{-2\xi_{\mathrm{b}}})$. The interface coupling is quite clear in the linear solutions, the amplitude of k_{a}-mode perturbation is affected by u_{a}, while l_{b} determines the amplitude of k_{b}-mode perturbation. When identical perturbation wavelengths are imposed at the upper and lower interfaces, it is possible to suppress the growing modes by adjusting the initial perturbations at these interfaces.[18] However, this phenomenon does not occur when the initial perturbation wavelengths are different.

In the WN regime, mode-coupling between the two waves excites many waves with wave numbers $k_+ = k_{\mathrm{a}} + k_{\mathrm{b}}$, $k_- = k_{\mathrm{a}} - k_{\mathrm{b}}$, $2k_{\mathrm{a}}$, and $2k_{\mathrm{b}}$. For the second-order $O(\varepsilon^2)$, the coupled equations for $\eta_2^{\mathrm{u},+}$ and $\eta_2^{\mathrm{l},+}$ are

$$\frac{\mathrm{d}^2\eta_2^{\mathrm{u},+}}{\mathrm{d}t^2} - \frac{2\mathrm{e}^{-\xi_+}}{1+\mathrm{e}^{-2\xi_+}}\frac{\mathrm{d}^2\eta_2^{\mathrm{l},+}}{\mathrm{d}t^2} + \gamma_+^2\frac{1-\mathrm{e}^{-2\xi_+}}{1+\mathrm{e}^{-2\xi_+}}\eta_2^{\mathrm{u},+} + \gamma_+^2\Xi_{\mathrm{a}}\Xi_{\mathrm{b}}\,\mathrm{e}^{-\xi_{\mathrm{b}}}\Big[\mathrm{e}^{-2\xi_{\mathrm{a}}}f_1\cosh(\Gamma_{\mathrm{a}})\cos(\Gamma_{\mathrm{b}}) - f_2\cos(\Gamma_{\mathrm{a}})\cosh(\Gamma_{\mathrm{b}})$$
$$+ f_3\left(\mathrm{e}^{-2\xi_{\mathrm{a}}}\sinh(\Gamma_{\mathrm{a}}) - \sin(\Gamma_{\mathrm{a}})\right)\left(\sinh(\Gamma_{\mathrm{b}}) - \sin(\Gamma_{\mathrm{b}})\right)\Big], \quad (19)$$

$$\frac{\mathrm{d}^2\eta_2^{\mathrm{l},+}}{\mathrm{d}t^2}-\frac{2\mathrm{e}^{-\xi_+}}{1+\mathrm{e}^{-2\xi_+}}\frac{\mathrm{d}^2\eta_2^{\mathrm{u},+}}{\mathrm{d}t^2}-\gamma_+^2\frac{1-\mathrm{e}^{-2\xi_+}}{1+\mathrm{e}^{-2\xi_+}}\eta_2^{\mathrm{l},+}-\gamma_+^2\Xi_\mathrm{a}\Xi_\mathrm{b}\mathrm{e}^{-\xi_\mathrm{a}}\Big[\mathrm{e}^{-2\xi_\mathrm{b}}f_2\cosh(\Gamma_\mathrm{a})\cos(\Gamma_\mathrm{b})-f_1\cos(\Gamma_\mathrm{a})\cosh(\Gamma_\mathrm{b})$$
$$+f_3\left(\sinh(\Gamma_\mathrm{a})-\sin(\Gamma_\mathrm{a})\right)\left(\sinh(\Gamma_\mathrm{b})-\mathrm{e}^{-2\xi_\mathrm{b}}\sin(\Gamma_\mathrm{b})\right)\Big], \tag{20}$$

where $\xi_+=\xi_\mathrm{a}+\xi_\mathrm{b}$, $\gamma_+=\sqrt{gk_+}$ and the coefficients f_1–f_5 are

$$f_1=\left[\left(1-\mathrm{e}^{-2\xi_\mathrm{b}}\right)k_\mathrm{a}-\mathrm{e}^{-2\xi_\mathrm{b}}\left(1-\mathrm{e}^{-2\xi_\mathrm{a}}\right)k_\mathrm{b}\right]/\left(1+\mathrm{e}^{-2\xi_+}\right), \tag{21}$$
$$f_2=\left[e^{-2\xi_\mathrm{a}}\left(1-\mathrm{e}^{-2\xi_\mathrm{b}}\right)k_\mathrm{a}-\left(1-\mathrm{e}^{-2\xi_\mathrm{a}}\right)k_\mathrm{b}\right]/\left(1+\mathrm{e}^{-2\xi_+}\right), \tag{22}$$
$$f_3=\sqrt{k_\mathrm{a}k_\mathrm{b}}\left(1-\mathrm{e}^{-2\xi_+}\right)/\left(1+\mathrm{e}^{-2\xi_+}\right), \tag{23}$$
$$f_4=\left(1-2e^{-2\xi_\mathrm{a}}+\mathrm{e}^{-2\xi_+}\right)/\left(1-\mathrm{e}^{-2\xi_+}\right), \tag{24}$$
$$f_5=\left(1-2e^{-2\xi_\mathrm{b}}+e^{-2\xi_+}\right)/\left(1-e^{-2\xi_+}\right). \tag{25}$$

The solutions can be obtained by solving the Eqs. (19) and (20) as

$$\eta_2^{u,+}=\frac{1}{2}\left(k_\mathrm{a}+k_\mathrm{b}\right)\Xi_\mathrm{a}\Xi_\mathrm{b}\mathrm{e}^{-\xi_\mathrm{b}}\Big[\mathrm{e}^{-2\xi_\mathrm{a}}\cosh(\Gamma_\mathrm{a})\cosh(\Gamma_\mathrm{b})-f_4\cos(\Gamma_\mathrm{a})\cosh(\Gamma_\mathrm{b})$$
$$-\mathrm{e}^{-2\xi_\mathrm{a}}f_5\cos(\Gamma_\mathrm{b})\cosh(\Gamma_\mathrm{a})-\cos(\Gamma_\mathrm{a})\cos(\Gamma_\mathrm{b})-2\mathrm{e}^{-2\xi_\mathrm{a}}\cosh(\Gamma_+)+2\cos(\Gamma_+)\Big], \tag{26}$$
$$\eta_2^{\mathrm{l},+}=\frac{1}{2}\left(k_\mathrm{a}+k_\mathrm{b}\right)\Xi_\mathrm{a}\Xi_\mathrm{b}\mathrm{e}^{-\xi_\mathrm{a}}\Big[\cosh(\Gamma_\mathrm{a})\cosh(\Gamma_\mathrm{b})+\mathrm{e}^{-2\xi_\mathrm{b}}f_4\cos(\Gamma_\mathrm{b})\cosh(\Gamma_\mathrm{a})$$
$$+f_5\cos(\Gamma_\mathrm{a})\cosh(\Gamma_\mathrm{b})-\mathrm{e}^{-2\xi_\mathrm{b}}\cos(\Gamma_\mathrm{a})\cos(\Gamma_\mathrm{b})-2\cosh(\Gamma_+)+2\mathrm{e}^{-2\xi_\mathrm{b}}\cos(\Gamma_+)\Big]. \tag{27}$$

The governing equations for $\eta_2^{\mathrm{u},-}$ and $\eta_2^{\mathrm{l},-}$ are expressed as

$$\frac{\mathrm{d}^2\eta_2^{\mathrm{u},-}}{\mathrm{d}t^2}-\frac{2\mathrm{e}^{-\xi_-}}{1+\mathrm{e}^{-2\xi_-}}\frac{\mathrm{d}^2\eta_2^{\mathrm{l},-}}{\mathrm{d}t^2}+\gamma_-^2\frac{1-\mathrm{e}^{-2\xi_-}}{1+\mathrm{e}^{-2\xi_-}}\eta_2^{\mathrm{l},-}-\gamma_-^2\Xi_\mathrm{a}\Xi_\mathrm{b}\mathrm{e}^{-\xi_\mathrm{b}}\Big[h_1\cos(\Gamma_\mathrm{a})\cos(\Gamma_\mathrm{b})-\mathrm{e}^{-2\xi_-}h_2\cosh(\Gamma_\mathrm{a})\cosh(\Gamma_\mathrm{b})$$
$$+h_3\left(\mathrm{e}^{-2\xi_\mathrm{a}}\sinh(\Gamma_\mathrm{a})-\sin(\Gamma_\mathrm{a})\right)\left(\sinh(\Gamma_\mathrm{b})-\sin(\Gamma_\mathrm{b})\right)\Big], \tag{28}$$
$$\frac{\mathrm{d}^2\eta_2^{\mathrm{l},-}}{\mathrm{d}t^2}-\frac{2\mathrm{e}^{-\xi_-}}{1+\mathrm{e}^{-2\xi_-}}\frac{\mathrm{d}^2\eta_2^{\mathrm{u},-}}{\mathrm{d}t^2}-\gamma_-^2\frac{1-\mathrm{e}^{-2\xi_-}}{1+\mathrm{e}^{-2\xi_-}}\eta_2^{\mathrm{l},-}+\gamma_-^2\Xi_\mathrm{a}\Xi_\mathrm{b}\mathrm{e}^{-\xi_\mathrm{a}}\Big[h_2\cos(\Gamma_\mathrm{a})\cos(\Gamma_\mathrm{b})-h_1\cosh(\Gamma_\mathrm{a})\cosh(\Gamma_\mathrm{b})$$
$$+h_3\left(\sinh(\Gamma_\mathrm{a})-\sin(\Gamma_\mathrm{a})\right)\left(\sinh(\Gamma_\mathrm{b})-\mathrm{e}^{-2\xi_\mathrm{b}}\sin(\Gamma_\mathrm{b})\right)\Big], \tag{29}$$

where $\xi_-=\xi_\mathrm{a}-\xi_\mathrm{b}$, $\gamma_-=\sqrt{gk_-}$ and the coefficients h_1–h_5 are

$$h_1=\left[\mathrm{e}^{-2\xi_-}\left(1-\mathrm{e}^{-2\xi_\mathrm{b}}\right)k_\mathrm{a}-\left(1-\mathrm{e}^{-2\xi_\mathrm{a}}\right)k_\mathrm{b}\right]/\left(1+\mathrm{e}^{-2\xi_-}\right), \tag{30}$$
$$h_2=\left[\left(1-\mathrm{e}^{-2\xi_\mathrm{b}}\right)k_\mathrm{a}-\left(1-\mathrm{e}^{-2\xi_\mathrm{a}}\right)k_\mathrm{b}\right]/\left(1+\mathrm{e}^{-2\xi_-}\right), \tag{31}$$
$$h_3=\sqrt{k_\mathrm{a}k_\mathrm{b}}\left(1-\mathrm{e}^{-2\xi_-}\right)/\left(1+\mathrm{e}^{-2\xi_-}\right), \tag{32}$$
$$h_4=\left(1-2\mathrm{e}^{-2\xi_\mathrm{a}}+\mathrm{e}^{-2\xi_-}\right)/\left(1-\mathrm{e}^{-2\xi_-}\right), \tag{33}$$
$$h_5=\left(2-\mathrm{e}^{-2\xi_\mathrm{a}}-\mathrm{e}^{-2\xi_\mathrm{b}}\right)/\left(1-\mathrm{e}^{-2\xi_-}\right). \tag{34}$$

The solutions for $\eta_2^{\mathrm{u},-}$ and $\eta_2^{\mathrm{l},-}$ can be obtained by solving the above equations as

$$\eta_2^{\mathrm{u},-}=\frac{1}{2}\left(k_\mathrm{a}-k_\mathrm{b}\right)\Xi_\mathrm{a}\Xi_\mathrm{b}\mathrm{e}^{-\xi_\mathrm{b}}\Big[\cos\left(\Gamma_\mathrm{a}\right)\cosh\left(\Gamma_\mathrm{b}\right)-\mathrm{e}^{-2\xi_\mathrm{a}}\cos\left(\Gamma_\mathrm{b}\right)\cosh\left(\Gamma_\mathrm{a}\right)$$
$$+h_4\cos\left(\Gamma_\mathrm{a}\right)\cos\left(\Gamma_\mathrm{b}\right)-h_5\mathrm{e}^{-2\xi_-}\cosh\left(\Gamma_\mathrm{a}\right)\cosh\left(\Gamma_\mathrm{b}\right)+2\mathrm{e}^{-2\xi_\mathrm{a}}\cosh\left(\Gamma_-\right)-2\cos\left(\Gamma_-\right)\Big], \tag{35}$$
$$\eta_2^{\mathrm{l},-}=\frac{1}{2}\left(k_\mathrm{a}-k_\mathrm{b}\right)\Xi_\mathrm{a}\Xi_\mathrm{b}\mathrm{e}^{-\xi_\mathrm{a}}\Big[\cos\left(\Gamma_\mathrm{a}\right)\cosh\left(\Gamma_\mathrm{b}\right)-\mathrm{e}^{-2\xi_\mathrm{b}}\cos\left(\Gamma_\mathrm{b}\right)\cosh\left(\Gamma_\mathrm{a}\right)$$
$$-h_4\cosh\left(\Gamma_\mathrm{a}\right)\cosh\left(\Gamma_\mathrm{b}\right)+h_5\cos\left(\Gamma_\mathrm{a}\right)\cos\left(\Gamma_\mathrm{b}\right)+2\mathrm{e}^{-2\xi_\mathrm{b}}\cosh\left(\Gamma_-\right)-2\cos\left(\Gamma_-\right)\Big]. \tag{36}$$

The perturbation amplitudes for mode $2k_{\rm a}$ and $2k_{\rm b}$ at the two interfaces are

$$\eta_2^{{\rm u},2k_{\rm a}} = \frac{1}{2}k_{\rm a}\Xi_{\rm a}^2\left[\cos^2(\Gamma_{\rm a}) - {\rm e}^{-4\xi_{\rm a}}\cosh^2(\Gamma_{\rm a}) + 2{\rm e}^{-2\xi_{\rm a}}\frac{1-{\rm e}^{-2\xi_{\rm a}}}{1+{\rm e}^{-2\xi_{\rm a}}}\cos(\Gamma_{\rm a})\cosh(\Gamma_{\rm a})\right.$$
$$\left. + {\rm e}^{-4\xi_{\rm a}}\frac{3+{\rm e}^{-2\xi_{\rm a}}}{1+{\rm e}^{-2\xi_{\rm a}}}\cosh(\sqrt{2}\Gamma_{\rm a}) - \frac{1+3{\rm e}^{-2\xi_{\rm a}}}{1+{\rm e}^{-2\xi_{\rm a}}}\cos(\sqrt{2}\Gamma_{\rm a})\right], \tag{37}$$

$$\eta_2^{{\rm l},2k_{\rm a}} = -\frac{1}{2}k_{\rm a}\Xi_{\rm a}^2{\rm e}^{-2\xi_{\rm a}}\left[\cosh^2(\Gamma_{\rm a}) - \cos^2(\Gamma_{\rm a}) + \frac{2-2{\rm e}^{-2\xi_{\rm a}}}{1+{\rm e}^{-2\xi_{\rm a}}}\cos(\Gamma_{\rm a})\cosh(\Gamma_{\rm a})\right.$$
$$\left. - \frac{3+{\rm e}^{-2\xi_{\rm a}}}{1+{\rm e}^{-2\xi_{\rm a}}}\cosh(\sqrt{2}\Gamma_{\rm a}) + \frac{1+3{\rm e}^{-2\xi_{\rm a}}}{1+{\rm e}^{-2\xi_{\rm a}}}\cos(\sqrt{2}\Gamma_{\rm a})\right], \tag{38}$$

$$\eta_2^{{\rm u},2k_{\rm b}} = \frac{1}{2}k_{\rm b}\Xi_{\rm b}^2{\rm e}^{-2\xi_{\rm b}}\left[\cos^2(\Gamma_{\rm b}) - \cosh^2(\Gamma_{\rm b}) + 2\frac{1-{\rm e}^{-2\xi_{\rm b}}}{1+{\rm e}^{-2\xi_{\rm b}}}\cos(\Gamma_{\rm b})\cosh(\Gamma_{\rm b})\right.$$
$$\left. + \frac{1+3{\rm e}^{-2\xi_{\rm b}}}{1+{\rm e}^{-2\xi_{\rm b}}}\cosh(\sqrt{2}\Gamma_{\rm b}) - \frac{3+{\rm e}^{-2\xi_{\rm b}}}{1+{\rm e}^{-2\xi_{\rm b}}}\cos(\sqrt{2}\Gamma_{\rm b})\right], \tag{39}$$

$$\eta_2^{{\rm l},2k_{\rm b}} = -\frac{1}{2}k_{\rm b}\Xi_{\rm b}^2\left[\cosh^2(\Gamma_{\rm b}) - {\rm e}^{-4\xi_{\rm b}}\cos^2(\Gamma_{\rm b}) + 2{\rm e}^{-2\xi_{\rm b}}\frac{1-{\rm e}^{-2\xi_{\rm b}}}{1+{\rm e}^{-2\xi_{\rm b}}}\cos(\Gamma_{\rm b})\cosh(\Gamma_{\rm b})\right.$$
$$\left. + {\rm e}^{-4\xi_{\rm b}}\frac{3+{\rm e}^{-2\xi_{\rm b}}}{1+{\rm e}^{-2\xi_{\rm b}}}\cos(\sqrt{2}\Gamma_{\rm b}) - \frac{1+3{\rm e}^{-2\xi_{\rm b}}}{1+{\rm e}^{-2\xi_{\rm b}}}\cosh(\sqrt{2}\Gamma_{\rm b})\right], \tag{40}$$

when the initial wavelengths at the two interfaces are identical ($k_{\rm a} = k_{\rm b}$), the WN solutions for single-mode perturbations of finite-thickness shell is recovered.[26]

3. Numerical simulation

To simulate the weakly nonlinear interaction of the double-interface coupling obtained in Section 2, we use an Euler-based fluid simulation code.[29] The hydrodynamics are governed by the ideal gas equation of state, with a CFL number set to 0.3. This study adopts a two-dimensional Cartesian grid using a single-temperature, single-fluid model to investigate the coupling effects of two interfaces at different thicknesses. The governing equations are as follows:

$$\frac{\partial\rho}{\partial t} + \nabla\cdot(\rho\boldsymbol{u}) = 0, \tag{41}$$

$$\frac{\partial(\rho\boldsymbol{u})}{\partial t} + \nabla\cdot(\rho\boldsymbol{u}\boldsymbol{u}) = -\nabla p + \rho\boldsymbol{g}, \tag{42}$$

$$\frac{\partial\rho E}{\partial t} + \nabla\cdot[(\rho E + p)\boldsymbol{u}] = \rho\boldsymbol{g}\cdot\boldsymbol{u}, \tag{43}$$

where ρ (in units g/cm^3) is the fluid density, $\boldsymbol{u}$ (in units cm/μs) represents the velocity vector, $\boldsymbol{g}$ is the gravitational acceleration, and p (in unit Mbar, 1 bar $= 10^5$ Pa) denotes the pressure. The pressure is given by $p = c_v(\Gamma-1)\rho T$, where T (in unit MK) is the temperature, c_v is the specific heat capacity at constant volume, and Γ is the specific heat ratio. The total energy is defined as $E = c_v\rho T + (1/2)\rho|\boldsymbol{u}|^2$. To simulate the incompressible fluids, we set $\Gamma = 10$ in the numerical simulations. Under this configuration, the pressure waves can propagate instantaneously throughout the fluid, and any local pressure change in the fluid will immediately spread throughout the entire fluid, leaving no time for the fluid to undergo volume changes, thus exhibiting incompressibility.

The computational domain in this study is set to $L\times 5L$, as illustrated in Fig. 1. The acceleration is applied in the vertical ($5L$) direction. To facilitate the observation of interface coupling effects, L is chosen to be twice the wavelength of the long-wavelength perturbation. The applied acceleration is 1000 cm/μs^2. Three different density configurations are considered for the upper and lower interface Atwood numbers. The density of the region between the two interfaces is fixed at 1 g/cm^3, while the upper and lower fluid layers have a density of 0.01 g/cm^3. The separation distance between the two interfaces is denoted as d. Periodic boundary conditions are applied in the x-direction maintain the consistency of the perturbation structures across the domain, while wall boundary conditions are applied in the y-direction. A uniform grid resolution is used, with a grid spacing of 0.2 μm in the x-direction and 1 μm in the y-direction.

To ensure accurate interface tracking, the initial perturbation region is refined using a weighted averaging subdivision method, where each grid cell is divided into 100 subcells. This approach enhances interface resolution and reduces numerical diffusion. The refinement is applied at $t = 0$ to ensure a well-defined perturbation structure, particularly in cases where interface instability plays a crucial role in the evolution. The numerical scheme employs a finite-volume method with large-scale parallel computation. A second-order HLLE ap-

proximate Riemann solver[30] is used, along with a Moncen slope limiter[31] to enhance solution accuracy and numerical stability. The initial velocity field is set to zero, and a cosinusoidal perturbation with an amplitude of 0.01λ is imposed at both interfaces.

4. Results and discussion

In this section, we systematically investigate the growth of RTI at the upper and lower interfaces with different initial perturbation modes and analyze the evolution of the perturbation at both interfaces. Two representative configurations are considered: (i) initial perturbations of dissimilar wavelengths with wave number $k_a/k_b > 2$ (representing long-range coupling effects), and (ii) initial perturbations of similar wavelengths with $k_a/k_b < 2$ (characterizing short-range interactions). To validate the reliability of the analytical results, we perform a series of numerical simulations.

4.1. Weakly nonlinear evolution

The shell-thickness $k_a d$ dependence of the evolution of the upper and lower interfaces is displayed in Fig. 2.

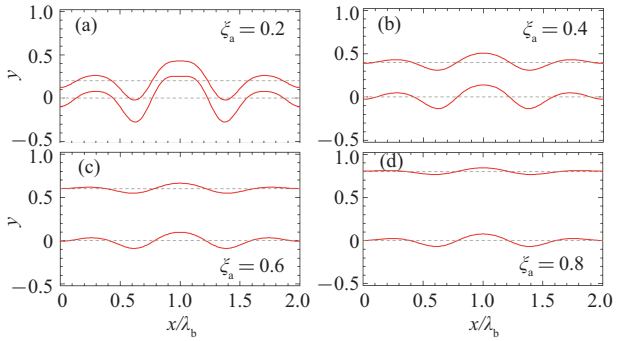


Fig. 2. Temporal evolution of positions of the upper and lower interfaces of the finite-thickness shell at $\Gamma_b t = 4$ for shell thickness $\xi_a = 0.2$ (a), 0.4 (b), 0.6 (c), and 0.8 (d). The initial perturbation modes at the two interfaces are $k_a = 3$ and $k_b = 2$, respectively.

The initial perturbation amplitudes at the upper and lower interfaces are $u_a = 0.001\lambda_a$ and $l_b = 0.001\lambda_b$, and the initial perturbation modes are $k_a = 3$ and $k_b = 2$. Thus, the positions of the upper and lower interfaces for $k_a d = 0.2$, 0.4, 0.6, and 0.8 at $\Gamma_b t = 4$ can be obtained through the WN solutions. As the upper interface of the fluid layer is initially stable, whereas the lower interface is RT-unstable. For a thin shell (small $k_a d$), due to the coupling effect between the upper and lower interfaces, the upper interface (initially stable) will become unstable. With time proceeding, the perturbation amplitude of the upper interface approximates to that of the lower interface, and the remarkable bubble-spike structure can be seen in Fig. 2(a). As the fluid thickness $k_a d$ increases, the coupling effect between two interfaces gradually weakens. Compared with the thin shell, the growth of the perturbation amplitudes at the interface of the thick shell ($k_a d = 0.8$) will be much smaller, which can be seen in Fig. 2(d).

4.2. Interaction of dissimilar wavelengths

In this section, we consider initial perturbations with dissimilar wavelengths at the upper and lower interfaces. The initial perturbation wavelength at the upper interface is 33.3π (in unit μm) for $k_a = 3$, while at the lower interface, it is 100π (in unit μm) for $k_b = 1$. The shell thickness is 10 μm.

Temporal evolution of the interface positions of a finite-thickness fluid layer is investigated when there are dissimilar wavelengths at the upper and lower interfaces. The Figs. 3(a)–3(d) are the theoretical results, and figures 3(a′)–3(d′) show the numerical simulation results under the same conditions. The perturbed interfaces are displayed at $t = 0$ ns [3(a), 3(a′)], 1.0 ns [3(b), 3(b′)], 1.5 ns [3(c), 3(c′)], and 2.0 ns [3(d), 3(d′)]. It can be seen that the analytical results are consistent with the numerical simulation results. With time proceeding, the long-wavelength perturbations at the lower interface can easily feed through to the upper interface, leading to the unstable growth of the upper interface. Subsequently, long-wavelength perturbations will dominate the instability growth of the upper interface. Due to the coupling effects among the interfaces, multi-mode coupling effects will manifest at two interfaces. The deformation of the bubble-spike structure is affected by the multi-mode coupling effects.

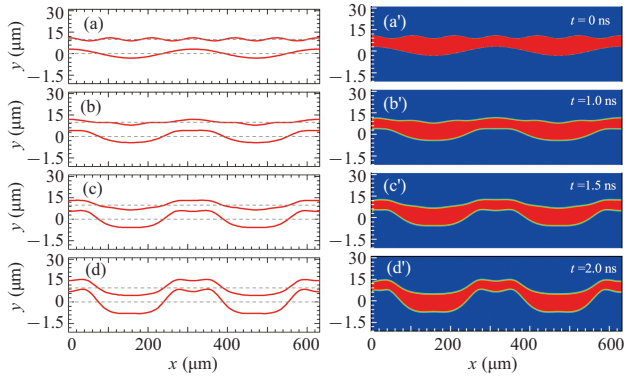


Fig. 3. Evolution of interface positions obtained by the present model (a)–(d), and numerical simulation (a′)–(d′) at the same time. The initial perturbation wavelengths at the upper and lower interfaces are $\lambda_a = 33.3\pi$ (μm) and $\lambda_b = 100\pi$ (μm), respectively.

In order to study the deformation of the fluid layer, we investigate the amplitude growth of the wave peak (the maximum value of perturbation) η^p and that of wave valley (the minimum value of perturbation) η^v at the two interfaces in Fig. 4, the numerical results are included for comparison. It can be seen that the theoretical results are consistent with the simulation results. With the time proceeding, the amplitudes of peak-to-valley $|\eta^p - \eta^v|$ grows quickly. It is clearly demonstrate that the perturbation amplitude growth rates at the upper and lower interfaces exhibit identical characteristics. This synchronization arises from the coupling of long-wavelength perturbations originating at the lower interface to the upper interface, which dominate the primary growth mechanism of the upper interface.

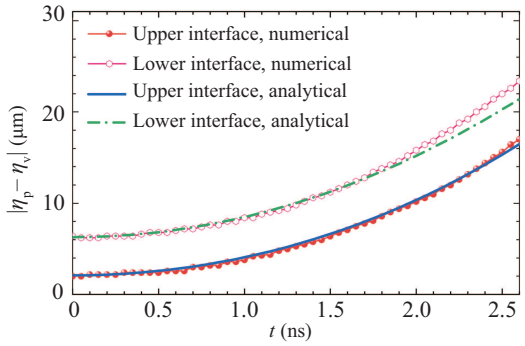


Fig. 4. Comparisons of the temporal evolution of the maximum peak-to-valley amplitude at the upper and lower interfaces between the WN model (lines) and the numerical results (symbols). The initial conditions are identical to those in Fig. 3.

In the previous weakly nonlinear models, the initial perturbation wavelengths at the upper and lower interfaces of the shell were the same with $k_a = k_b$, which can be referred to as single-mode perturbations. Figure 5 illustrates a comparison between the positions of the fluid interface obtained from the present model (represented by solid lines) and the single-mode model (depicted by dotted lines) at $t = 0$ ns, 1.1 ns, and 2.2 ns. In the present model, the initial perturbation wavelengths are $\lambda_a = 33.3\pi$ (μm) and $\lambda_b = 100\pi$ (μm). In the single-mode perturbation model, the initial perturbation wavelengths are equal with $\lambda_a = \lambda_b = 100\pi$ (μm). It can be observed that the main structure of the bubble-spike is consistent with that of the single-mode model in Fig. 3.

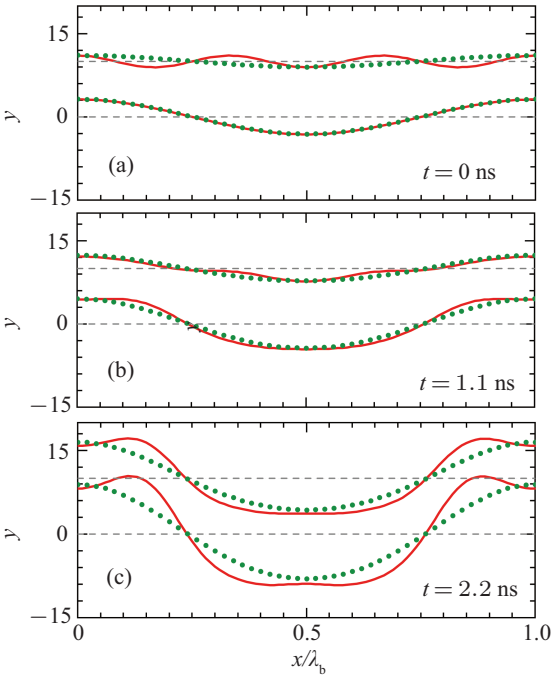


Fig. 5. Comparisons of the WN model (lines) with the single-mode model (dotted) for $d = 10$ (μm) at $t = 0$ ns (a), 1.1 ns (b), and 2.2 ns (c). The initial perturbation wavelengths at the upper and lower interfaces are $\lambda_a = 33.3\pi$ (μm) and $\lambda_b = 100\pi$ (μm) for WN model, and the wavelengths at both interfaces are the same ($\lambda = \lambda_b$) for single-mode model.

However, there are significant differences in the interface positions obtained by the present model and the single-mode model. In the present model, the shapes of the bubbles and the spikes will broaden more significantly. The interfacial coupling effects induce simultaneous excitation of two primary modes at the upper and lower interfaces, leading to the formation of multi-mode perturbation structures in both bubble and spike regions. Thus, the initially different perturbation wavelengths at the shell interfaces will lead to more severe interface deformations. Therefore, in the prediction of the deformation of the ICF implosion, the initial perturbation wavelengths at different interfaces must be taken into account.

Temporal evolution of fundamental modes $\eta_1^{i,a}/\lambda_b$ and $\eta_1^{i,b}/\lambda_b$ is shown in Fig. 6. Here, the superscript indices i are used to denote the upper (u) and lower (l) interfaces. It can be seen in Eq. (17), there is a π-phase shift in the perturbation of the lower interface compared to the initial phase configuration at the upper interface. Moreover, this phase reversal phenomenon is also evident in Fig. 6. For the dissimilar case where the perturbation wavelengths are not close, the lower interface has a long-wavelength perturbation λ_b, while the upper interface has a short-wavelength perturbation. The long-wavelength perturbation grows rapidly and can easily couple to the upper interface, triggering the growth of perturbations at the upper interface. Then, it dominates the growth of perturbations at the upper interface. Thus, the main structure of the bubble-spike is consistent with that in the single-mode case.

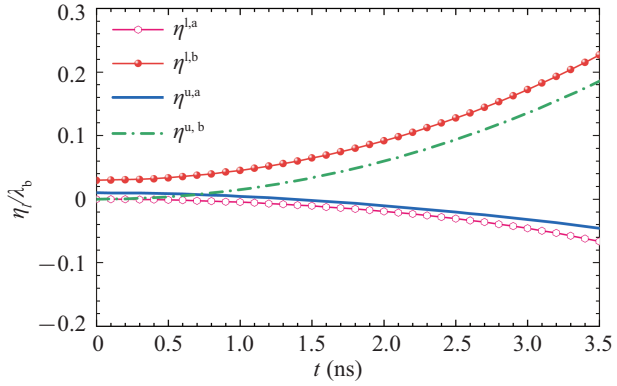


Fig. 6. Temporal evolution of fundamental modes $\eta_1^{i,a}/\lambda_b$ and $\eta_1^{i,b}/\lambda_b$ at the upper and lower interfaces. The initial conditions are the same as those in Fig. 3.

Due to the coupling effect between interfaces, perturbations initially at one interface will couple to the other, resulting in mode-coupling effects at both interfaces. Thus, the perturbations of sum frequency mode $k_a + k_b$ and difference frequency mode $k_a - k_b$ are generated. In Fig. 7, it can be seen that as time increases, the amplitude of the sum frequency at the lower interface will gradually become larger than that of the perturbation at the upper interface. The difference frequency amplitudes at the upper and lower interfaces are slightly different. In addition, the phases of the difference frequency mode and the sum frequency mode are the same, which is different from the classical RTI, where the phases of

the difference frequency mode and the sum frequency mode are opposite.

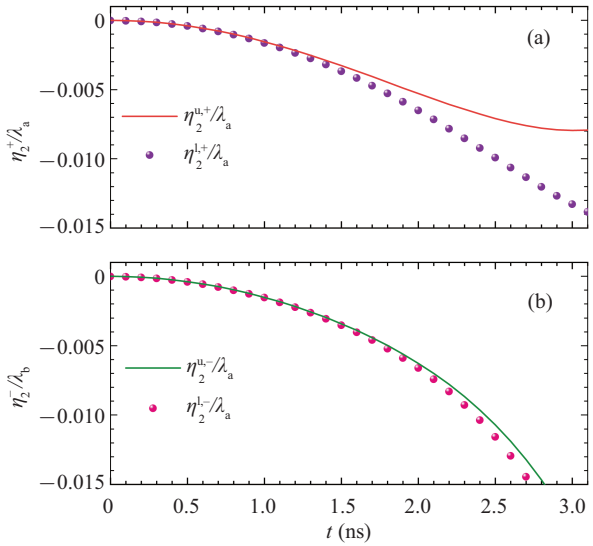


Fig. 7. The temporal evolution of sum frequency amplitudes $\eta_2^{i,+}/\lambda_a$ (a) and difference frequency amplitude $\eta_2^{i,-}/\lambda_a$ (b) at the upper and lower interfaces. The initial conditions are the same as those in Fig. 3.

4.3. Interaction of similar wavelengths

The perturbations with initial similar wavelengths at the upper and lower interfaces are discussed in this section, where the initial perturbation wavelength of the upper interface is 60π (in unit μm) for $k_a = 4$, and that of the lower interface is 80π (μm) for $k_b = 3$. The shell thickness is 10 μm.

Figure 8 shows the temporal evolution of the interface positions of a finite-thickness fluid layer when there are similar wavelengths at the initial upper and lower interfaces.

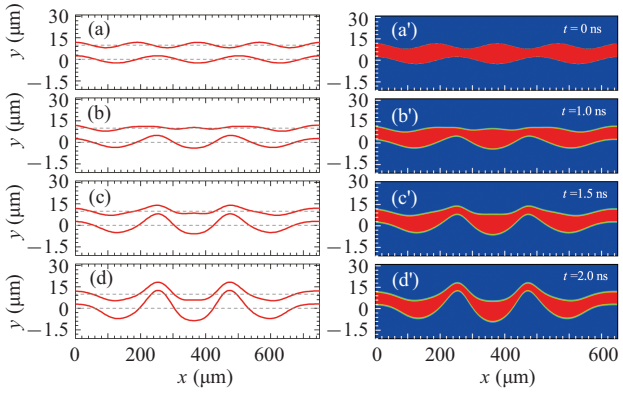


Fig. 8. Evolution of interface positions obtained by the present model (a)–(d), and numerical simulation (a′)–(d′) at the same time. The initial perturbation wavelengths at the upper and lower interfaces are $\lambda_a = 60\pi$ (μm) and $\lambda_b = 80\pi$ (μm), respectively.

Figures 8(a)–(d) are the theoretical results, and figures 8(a′)–(d′) show the numerical simulation results under same conditions. It can be clearly observed that the analytical results are in good agreement with the numerical simulation results. In contrast to the scenario with dissimilar wavelengths, when the perturbation wavelengths at the two interfaces are similar, irregular bubble-spike structures arise at both the upper and lower interfaces. In this case, the coupling of the perturbation wavelength at the upper interface to the lower interface, together with the effect of the initial perturbation at the lower interface, plays a significant role in the deformation of the shell. The bubble structure will transform to be relatively narrow, and the spike structure will become rounder. Consequently, the thickness within the bubble zone will decrease, while the thickness at the spike's location will increase.

Figure 9 illustrates the temporal evolution of the maximum values of the peak-to-valley amplitudes $|\eta^p - \eta^v|$ at the upper and lower interfaces when the initial perturbation wavelengths are close to each other. The perturbation amplitude at the lower interface exhibits a rapid growth. However, the perturbation at the upper interface initially experiences a gradual decline and subsequently starts to increase. Due to the fact that the upper interface is initially stable and the perturbation wavelengths at the upper and lower interfaces are different, the perturbation at the lower interface will be transmitted to the upper interface, causing the initial wave peak of the perturbation at the upper interface to decrease. Then, it gradually becomes consistent with the growth of the perturbation at the lower interface.

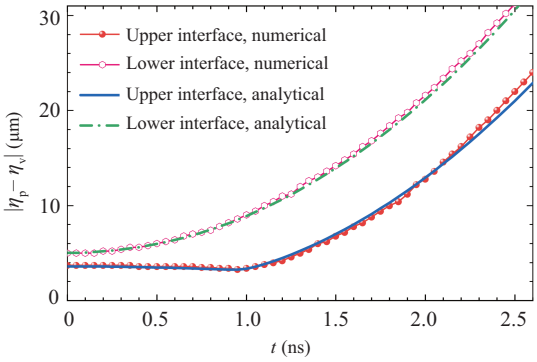


Fig. 9. Comparisons of the temporal evolution of the maximum peak-to-valley amplitude at the upper and lower interfaces between the WN model (lines) and the numerical results (symbols). The initial conditions are the same as those in Fig. 8.

Figure 10 exhibits the evolution of the interface positions obtained from the present model and the single-mode model. Here, the initial perturbation wavelengths are $\lambda_a = 60\pi$ (μm) at the upper interface and $\lambda_b = 80\pi$ (μm) at the lower interface. In the single-mode perturbation model, the initial perturbation wavelengths are identical with $\lambda_a = \lambda_b = 80\pi$ (μm). It can be observed that the main structure of the bubble-spike is different from that of the single-mode model. When the perturbation at the upper interface couples with that of the lower interface, the similar perturbation wavelengths trigger a mode-coupling effect. As a result, the positions of the bubble-spike deviate from their initial positions. However, in the case of single-mode perturbation, the positions of the bubble-spike remain unchanged. Despite the disparity in the initial perturbation wavelengths of the upper and lower interfaces, due to the interface coupling effect, the position of the upper interface

will gradually align with that of the lower interface. As can also be seen in Fig. 10, when the initial perturbation wavelengths at the two interfaces are similar, the growth of bubbles and spikes becomes more severe. The bubble regions will narrow, and the spike regions will assume a more rounded shape. This will lead the shell layer to undergo substantial deformation.

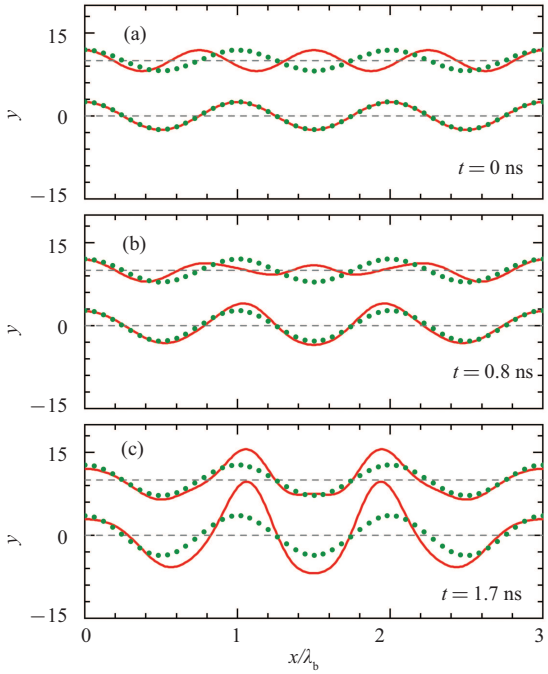


Fig. 10. Comparisons of the present model (lines) with the single-mode model (dotted) with $d = 10$ μm at $t = 0$ ns (a), 0.8 ns (b), and 1.7 ns (c). The initial perturbation wavelengths at the upper and lower interfaces are $\lambda_a = 60\pi$ (μm) and $\lambda_b = 80\pi$ (μm) for WN model, and the wavelengths at both interfaces are the same ($\lambda = \lambda_b$) for single-mode model.

Temporal evolution of fundamental modes $\eta_1^{i,a}/\lambda_b$ and $\eta_1^{i,b}/\lambda_b$ is displayed in Fig. 11. Here, the initial perturbation wavelengths at the two interfaces are similar. Since the initial perturbation wavelengths are similar, the amplitudes of the perturbation with wavelength of 60π (μm) and that with wavelength of 80π (μm) are nearly identical. In combination, they exert a predominant influence on the structure of both the bubbles and spikes, along with the deformation of the interface.

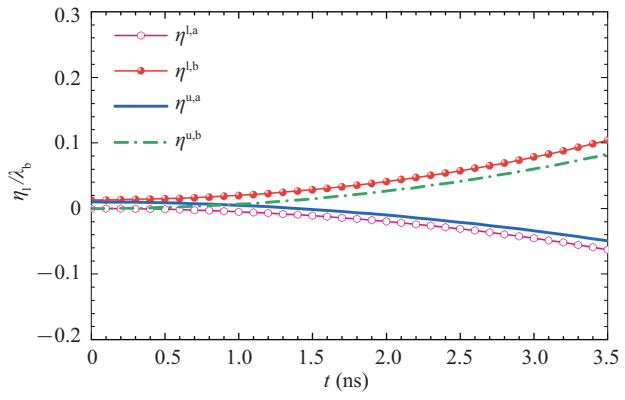


Fig. 11. The temporal evolution of fundamental modes $\eta_1^{i,a}/\lambda_b$ and $\eta_1^{i,b}/\lambda_b$ at the upper and lower interfaces. The initial conditions are the same as those in Fig. 8.

As shown in Fig. 12, the perturbation amplitudes generated by the interaction of similar wavelengths are smaller than those generated by dissimilar wavelengths. It can be seen in Eqs. (35) and (36), the coupling coefficient between the interfaces for difference frequency $\eta_2^{i,-}$ is $e^{-\xi_-}$. When initial perturbation wavelengths are $\lambda_a = 60\pi$ (μm) and $\lambda_b = 80\pi$ (μm), the coupling coefficient is close to 0.92. Thus, the difference frequency amplitudes at the two interfaces are nearly identical.

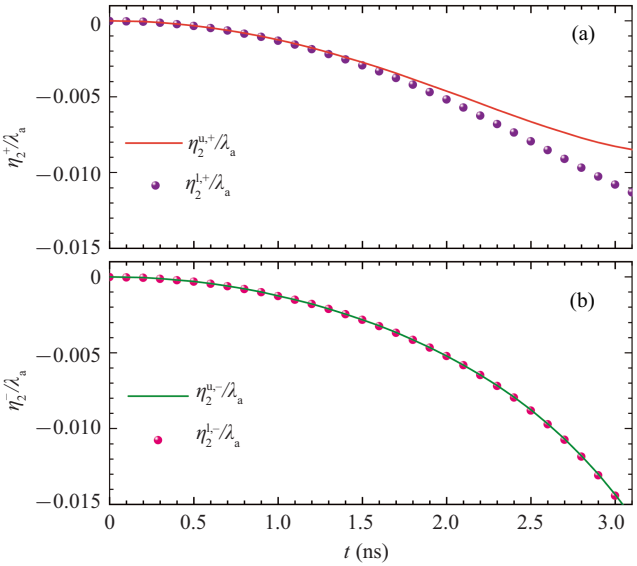


Fig. 12. The temporal evolution of sum frequency amplitudes $\eta_2^{i,+}/\lambda_a$ (a) and difference frequency amplitude $\eta_2^{i,-}/\lambda_a$ (b) at the upper and lower interfaces. The initial conditions are the same as those in Fig. 8.

5. Conclusion

In this study, we developed a WN model based on the potential flow theory of ideal incompressible fluids. The model can describe the RTI growth of a finite-thickness shell, where the upper and lower interfaces are perturbed with different initial perturbation wavelengths. When the initial perturbation wavelengths at the two interfaces are identical, the previous single-mode results for the RTI growth of a finite-thickness slab are recovered.[26] We conducted numerical simulations, employing the second-order HLLE Riemann solver and the Moncen slope limiter. The analytical results are in excellent agreement with the numerical simulation results. When the upper and lower interfaces are initially subjected to dissimilar wavelengths, owing to the coupling effect between two interfaces, the initial single-mode perturbation at the upper and lower interfaces will manifest a multi-mode coupling growth phenomenon during the growth progression. The main structure of the bubble-spike is dominated by the long-wavelength perturbation, which is consistent with the characteristics of single-mode perturbations, the deformations of the bubbles and spikes will be significantly influenced by the mode-coupling effect. When the initial perturbation wavelengths at the upper and lower interfaces are similar, due to the

mode-coupling effect, the positions of the bubbles and spikes will change significantly, and the growth of the bubbles and spikes will become more severe. The analytical model is expected to enhance the understanding of the nonlinear growth of the RTI in finite-thickness shells. Our model can be used to quantify the extent to which external perturbations penetrate to the hot-spot interface and predict the most dangerous perturbation wavelengths during the implosion of thin shells in ICF.

Acknowledgements

Project supported by the Fundamental Research Funds for the Central Universities (Grant No. 2022YQLX01), the Fund from the State Key Laboratory of Computational Physics (Grant No. 6142A05QN23009), and the Strategic Priority Research Program of the Chinese Academy of Sciences (Grant No. XDA 25051000).

References

[1] Rayleigh L 1882 *Proc. London Math. Soc.* **s1–14** 170
[2] Taylor G 1950 *Proc. R. Soc. Lond. A* **201** 192
[3] Gamezo V N, Khokhlov A M, Oran E S, Chtchelkanova A Y and Rosenberg R O 2003 *Science* **299** 77
[4] Lindl J D, Amendt P, Berger R L, Glendinning S G, Glenzer S H, Haan S W, Kauffman R L, Landen O L and Suter L J 2004 *Phys. Plasmas* **11** 339
[5] Wang L F, Ye W H, He X T, Wu J F, Fan Z F, Xue C, Guo H Y, Miao W Y, Yuan Y T, Dong J Q, Jia G, Zhang J, Li Y J, Liu J, Wang M, Ding Y K and Zhang W Y 2017 *Sci. China-Phys. Mech. Astron.* **60** 055201
[6] Zylstra A B, Hurricane O A, Callahan D A, *et al.* 2022 *Nature* **601** 542
[7] Guo Y, Wu D and Zhang J 2024 *Phys. Plasmas* **31** 112106
[8] Li J, Yan R, Zhao B, Wu J F, Wang L F and Zou S Y 2024 *Phys. Plasmas* **31** 012703
[9] Jacobs J W and Catton I 1988 *J. Fluid Mech.* **187** 329
[10] Liu W H, Wang L F, Ye W H and He X T 2012 *Phys. Plasmas* **19** 042705
[11] Wang L F, Wu J F, Fan Z F, Ye W H, He X T, Zhang W Y, Dai Z S, Gu J F and Xue C 2012 *Phys. Plasmas* **19** 112706
[12] Wang L F, Wu J F, Ye W H, Zhang W Y and He X T 2013 *Phys. Plasmas* **20** 042708
[13] Zhang J, Wang L F, Ye W H, Wu J F, Guo H Y, Zhang W Y and He X T 2017 *Phys. Plasmas* **24** 062703
[14] Lai H L, Xu A G, Zhang G C, Gan Y B, Ying Y J and Sauro Succi 2016 *Phys. Rev. E* **94** 023106
[15] Xin J, Yan R, Wan Z H, Sun J, Zheng J, Zhang H, Aluie H and Betti R 2019 *Phys. Plasmas* **26** 032703
[16] Mikaelian K O 1982 *Phys. Rev. A* **26** 2140
[17] Mikaelian K O 1983 *Phys. Rev. A* **28** 1637
[18] Mikaelian K O 2025 *Phys. Fluids* **37** 032114
[19] Guo H Y, Wang L F, Ye W H, Wu J F and Zhang W Y 2017 *Chin. Phys. Lett.* **34** 075201
[20] Guo H Y, Wang L F, Ye W H, Wu J F and Zhang W Y 2017 *Chin. Phys. B* **26** 125202
[21] Guo H Y, Wang L F, Ye W H, Wu J F, Li Y J and Zhang W Y 2018 *Chin. Phys. B* **27** 025206
[22] Weis M R, Zhang P, Lau Y Y, Rittersdorf I M, Zier J C, Gilgenbach R M and Peterson K J 2014 *Phys. Plasmas* **21** 122708
[23] Velikovich A L and Schmit P F 2015 *Phys. Plasmas* **22** 122711
[24] Wilkinson J P and Jacobs J W 2007 *Phys. Fluids* **19** 124102
[25] Ding J C, Si T, Yang J M, Lu X Y, Zhai Z G and Luo X S 2017 *Phys. Rev. Lett.* **119** 014501
[26] Wang L F, Guo H Y, Wu J F, Ye W H, Liu J, Zhang W Y and He X T 2014 *Phys. Plasmas* **21** 122710
[27] Guo H Y, Wang L F, Ye W H, Wu J F, Zhang J, Ding Y K, Zhang W Y and He X T 2017 *Phys. Plasmas* **24** 112708
[28] Guo H Y, Cheng T, Li J and Li Y J 2022 *Chin. Phys. B* **31** 035203
[29] Li Z Y, Wang L F, Wu J F and Ye W H 2020 *Acta Mech. Sin.* **36** 789
[30] Einfeldt B 1988 *SIAM Journal on Numerical Analysis* **25** 294
[31] Roe P L 1986 *Ann. Rev. Fluid Mech.* **18** 337